Journal of
Applied Crystallography
ISSN 0021-8898
Editor: **Anke R. Pyzalla**

Dynamical theory calculations of spin-echo resolved grazing-incidence scattering from a diffraction grating

Rana Ashkar, P. Stonaha, A. L. Washington, V. R. Shah, M. R. Fitzsimmons, B. Maranville, C. F. Majkrzak, W. T. Lee, W. L. Schaich and Roger Pynn

J. Appl. Cryst. (2010). **43**, 455–465

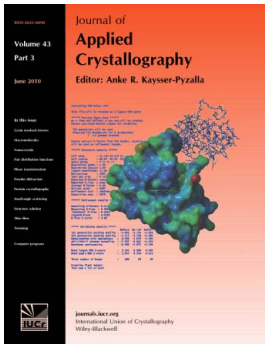

Journal of
Applied Crystallography
ISSN 0021-8898

Received 6 November 2009
Accepted 22 March 2010

Dynamical theory calculations of spin-echo resolved grazing-incidence scattering from a diffraction grating

Rana Ashkar,[a,b]* P. Stonaha,[a,b] A. L. Washington,[a,b] V. R. Shah,[c] M. R. Fitzsimmons,[d] B. Maranville,[e] C. F. Majkrzak,[e] W. T. Lee,[f] W. L. Schaich[b] and Roger Pynn[a,b,g]*

[a]Indiana University Center for the Exploration of Energy and Matter, Bloomington, IN 47408, USA, [b]Physics Department, Indiana University, Bloomington, IN 47405, USA, [c]Nebraska Center for Materials and Nanoscience, University of Nebraska, 111 Brace Laboratory, Lincoln, NE 68588, USA, [d]Los Alamos Neutron Science Center, Los Alamos, NM 87545, USA, [e]NIST Center for Neutron Research, Gaithersburg, MD 20899, USA, [f]Bragg Institute, Australian Nuclear Science and Technology Organization, Kirrawee DC NSW 2232, Australia, and [g]Neutron Science Directorate, Oak Ridge National Laboratory, Oak Ridge, TN 37831, USA. Correspondence e-mail: rashkar@indiana.edu, rpynn@indiana.edu

Neutrons scattered or reflected from a diffraction grating are subject to a periodic potential analogous to the potential experienced by electrons within a crystal. Hence, the wavefunction of the neutrons can be expanded in terms of Bloch waves and a dynamical theory can be applied to interpret the scattering phenomenon. In this paper, a dynamical theory is used to calculate the results of neutron spin-echo resolved grazing-incidence scattering (SERGIS) from a silicon diffraction grating with a rectangular profile. The calculations are compared with SERGIS measurements made on the same grating at two neutron sources: a pulsed source and a continuous wave source. In both cases, the spin-echo polarization, studied as a function of the spin-echo length, peaks at integer multiples of the grating period but there are some differences between the two sets of data. The dynamical theory explains the differences and gives a good account of both sets of results.

1. Introduction

Diffraction gratings have been used as samples for many radiation scattering experiments both to characterize their surfaces as well as to test new measurement techniques and schemes for calculating reflection and transmission properties. Early uses of gratings for these purposes were associated with the development of optical scattering techniques and of mathematical models to describe the behavior of electric and magnetic fields near conducting surfaces (Maystre & Petit, 1972; Neviere *et al.*, 1974). More recently, gratings have also served as standardized samples for more advanced probing techniques based on X-ray, electron and neutron scattering, in which the penetrating properties of the radiation and the interaction with the sample require more complicated scattering theories. With the enhancement of laser-based fabrication techniques over the past 20 years, good-quality gratings with various profiles and periods of ∼100 nm and greater have become readily available for such tests. In this paper we describe the use of a diffraction grating to test spin-echo resolved grazing-incidence scattering (SERGIS), a technique that is being developed at several neutron scattering centers (Felcher *et al.*, 2002; Bouwman *et al.*, 2005) to increase both the sensitivity and the accessible length scales probed by grazing-incidence neutron reflection.

SERGIS is an interferometric neutron scattering technique that makes use of neutron spin-echo coding along with the grazing-incidence scattering geometry to probe in-plane structures in thin films over a length scale that can extend from a few nanometres to a few micrometres. The upper end of this range is generally inaccessible to conventional grazing-incidence small-angle neutron scattering (GISANS) techniques because of neutron beam intensity limitations, although structures with length scales from 1 to 50 μm often give rise to diffuse scattering within the specular reflection plane and can be studied in this way. Unlike GISANS, which requires tight collimation of the neutron beam to achieve high in-plane wavevector transfer (q) resolution, SERGIS uses the neutron spin to encode, with high resolution, an in-plane component of the neutron wavevector transfer without requiring strong beam collimation and concomitant loss of signal intensity (Felcher *et al.*, 2002). Moreover, making use of the traditional advantages of neutron reflectometry, such as contrast enhancement and measurement of depth-dependent film structures, SERGIS can be used for structural characterization of patterned samples even when the buried morphology does

not extend to the free surface of the sample. In other simpler systems, it can be used as an effective complement to the traditional real-space techniques such as atomic force microscopy and scanning electron microscopy (SEM) in probing surfaces and providing a statistical average of the surface structure over a large area.

We used SERGIS to examine a bare silicon diffraction grating of period d = 140 nm, groove depth t = 65 nm and filling factor f = 1/2 obtained from LightSmyth Technologies (OR, USA)[1] (Fig. 1). Grazing-incidence reflection experiments were performed both at the Los Alamos Neutron Scattering Center (LANSCE) pulsed neutron source and at the NIST Center of Neutron Research (NCNR) reactor neutron source. The measured spin-echo polarization, which is determined by the grating structure, has several expected features such as peaks at integer multiples of the grating period, but the detailed results obtained at the two sources are different. In an attempt to understand the difference between the two sets of data, we have developed a dynamical theory based on Bloch wave expansion and used it to calculate the reflectivity from the grating and the resulting spin-echo polarization.

Several methods have been used in the past to calculate specular and diffuse neutron reflection from structured surfaces. In particular, the distorted wave Born approximation (DWBA) has been found to give a good account of diffuse neutron reflection from rough surfaces under certain conditions (Sinha *et al.*, 1988) and the phase-object approximation, originally developed to describe high-energy electron scattering, has also been used to describe both neutron reflection and transmission by gratings (de Haan *et al.*, 2007). In the case of the DWBA, one first calculates the solution of an idealized problem in which the physical structure of the reflecting surface is laterally averaged in some way. This *ideal* problem may comprise a single surface at the average height of the surface features or, in the case of a grating, may consist of a homogeneous layer atop a substrate. The DWBA is instructive in providing a sense of the scattering we might expect, because the approximation provides a clear, physically appealing result (Sinha *et al.*, 1988; Pynn, 1992), namely that the total scattering is given by the Fourier transform of the height–height correlation function of the grating surface times some optical coefficients that can be expressed in terms of the Fresnel reflectivity for an *ideal* system. Since SERGIS measures the cosine Fourier transform of the neutron scattering cross section (Major *et al.*, 2009; Krouglov *et al.*, 2003; Rekveldt *et al.*, 2005), the DWBA result implies that we should measure a signal that resembles the height autocorrelation function of the grating, provided the optical coefficients do not introduce a distortion. In particular, this model implies that we should detect peaks in the measured spin-echo polarization at integer multiples of the grating period which is, indeed, what we see (§4).

The phase-object approximation (POA) is a method first used in describing electron diffraction (Cowley & Moodie, 1957, 1959), which attempts to add multiple scattering effects to the simple kinematic (first-order Born) approximation by calculating the phase to be associated with each incident particle as that accumulated along its classical path. It is valid provided the particles are only scattered through very small angles (Jap & Glaeser, 1978). The POA has been applied to several cases of electron scattering, and it has been shown that the validity of this approximation is determined by the object thickness and the electron wavelength and that it breaks down for relatively thick samples. The limits of this approximation in neutron scattering have not been established clearly yet but it has given good fits to spin-echo small-angle neutron scattering data obtained in transmission experiments with diffraction gratings (de Haan *et al.*, 2007). It has also been used to explain the general features of the spin-echo polarization resulting from neutron reflection from sinusoidal gratings, although the calculations required adjustment of the grating period and groove depth (Plomp, 2009; Plomp *et al.*, 2007) to obtain adequate fits to experimental data. When neutrons are incident perpendicular to the surface of a diffraction grating, the maximum phase difference between waves propagating through ridges and valleys of the grating is $\sim\rho\lambda t$ (ρ is the scattering length density of the grating material, λ is the neutron wavelength and t is the depth of the grating features). This phase difference is roughly 1 milliradian for our grating in the transmission mode, but in reflection experiments the phase difference between waves reflected from the ridges and the grooves is $\sim$2.5 radians for our grating when the incident angle is close to the silicon critical angle. This large phase shift leads one to wonder whether the phase-object approximation holds in this case. In addition, in the reflection geometry the incident waves may be substantially distorted. For example, the grooves of the grating may act as waveguides for neutrons, so that waves with very large effective wavelength (*i.e.* those

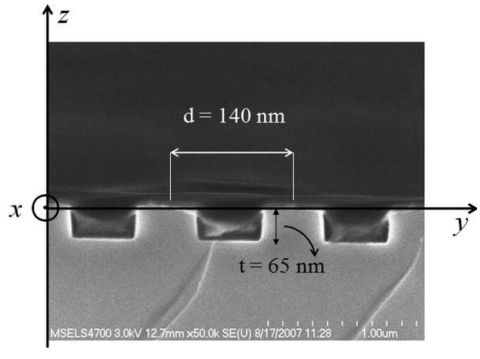

Figure 1
SEM image of the grating (as provided by LightSmyth Technologies) indicating a rectangular profile of the grating with a period of 140 nm, a groove depth of 65 nm and a filling factor f = 1/2. The x axis is chosen along the lines of the grating, the y axis is perpendicular to the lines and parallel to the surface, and the z axis is perpendicular to the average surface.

[1] Certain commercial equipment, instruments or materials (or suppliers or software *etc.*) are identified in this paper to foster understanding. Such identification does not imply recommendation or endorsement by the National Institute of Standards and Technology, nor does it imply that the materials or equipment identified are necessarily the best available for the purpose.

with very small wavevector components perpendicular to the average grating surface) may be unable to penetrate to the bottom of the grooves, rendering the classical-path approach suspect.

Dynamical theories based on Bloch wave expansion have been successfully applied to explain electron, X-ray and neutron reflection from diffraction gratings (Berrouane *et al.*, 1992; Humphreys, 1979; Ott *et al.*, 2001). Such theories acknowledge that multiple scattering results from the strong interaction between the incident beam and the scattering sample rendering the kinematic approximation an inadequate method for quantitative analysis. The dynamical theory was first developed to treat the scattering of electrons from crystals with periodic potential (Bethe, 1928). As in that case, the wavefunction of neutrons interacting with a grating can be expressed using a superposition of Bloch waves, and the amplitudes of the reflected and transmitted waves can be found by imposing the usual continuity conditions on the wavefunction and its derivatives at the layer boundaries. Gratings whose features are not rectangular (*e.g.* trapezoidal, triangular or sinusoidal) must be treated using a multi-slice dynamical approximation which requires dividing the system into many thin layers, each with a periodic rectangular-shaped scattering potential, and applying boundary conditions at the interfaces of all adjacent layers (Ott *et al.*, 2001). This method of dividing an arbitrary profile into many thin slices of well defined geometry is similar to the Parratt formalism (Parratt, 1954) that is widely used in the interpretation of X-ray and neutron measurements of specular reflectivity (Zabel, 1994; Vogt *et al.*, 2005; Hu *et al.*, 2005). Despite the complication of dynamical calculations on gratings with nonrectangular profiles, such gratings have been used for test experiments in the past mainly because sinusoidal or ruled gratings were the only ones available until relatively recently. With the development of laser-based fabrication techniques, different geometric profiles of gratings have become available. The simplest is the rectangular grating that we consider here.

In §2, the dynamical theory is used to obtain an expansion of the neutron wavefunctions above, below and within the grating. In the latter region, Bloch waves are used in the expansion. Applying the conventional boundary conditions on the wavefunction and its derivative allows an evaluation of the reflection and transmission amplitudes. These quantities determine the outcomes of the spin-echo polarization of a SERGIS experiment. In §3, we describe the SERGIS experimental setup. Experimental results obtained at continuous wave and pulsed neutron sources with the same grating are then compared in §4 with the dynamical theory calculations.

2. Dynamical theory

The interaction potential between neutrons and matter, $V(\mathbf{r})$, is proportional to the coherent scattering length density $\rho(\mathbf{r})$:

$$V(\mathbf{r}) = \frac{2\pi\hbar^2}{M}\rho(\mathbf{r}), \tag{1}$$

where $\hbar$ is the Planck constant and M is the mass of the neutron. Hence, neutrons whose wavevector in vacuum is $\mathbf{k}_0$ [*i.e.* which have kinetic energy $E_0 = (\hbar^2 k_0^2)/2M$] are described by a wavefunction, $\psi(\mathbf{r})$, that obeys the Schrödinger equation:

$$\nabla^2\psi(\mathbf{r}) + [k_0^2 - 4\pi\rho(\mathbf{r})]\psi(\mathbf{r}) = 0. \tag{2}$$

The experiment we consider here is one in which neutrons are incident on a diffraction grating at grazing incidence (described by θ) along a direction (described by φ) that is almost parallel to the rulings of the grating, as depicted in Figs. 2 and 3.

Figs. 1–3 define our coordinate system and show different projections of the diffraction process. Using the z axis as the polar axis of a spherical system and measuring the azimuthal angle from the xz plane, the incident wavevector is expressed as $\mathbf{k}_0 = (k_{0x}, k_{0y}, -k_{0z})$ with

$$\begin{aligned} k_{0x} &= k_0 \sin(\pi/2 - \theta)\cos\varphi \simeq k_0, \\ k_{0y} &= k_0 \sin(\pi/2 - \theta)\sin\varphi \simeq k_0\varphi, \\ k_{0z} &= k_0 \cos(\pi/2 - \theta) = k_0 \sin\theta \simeq k_0\theta, \end{aligned} \tag{3}$$

where $k_0 = 2\pi/\lambda$, λ is the neutron's wavelength in vacuum and θ is the incident angle with respect to the surface plane, which is a small angle in the case of grazing-incidence scattering

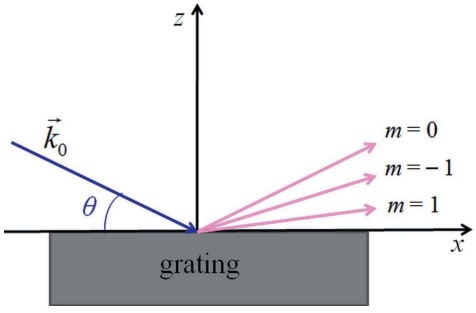

Figure 2
Projection of the incident and reflected neutron wavevectors on the xz plane (*cf.* Fig. 1) showing the neutron beam incident on the grating at a grazing angle θ with respect to the surface. Reflected beams of different diffraction orders, m, propagate away at different angles. The $m = 0$ wave corresponds to specular reflection.

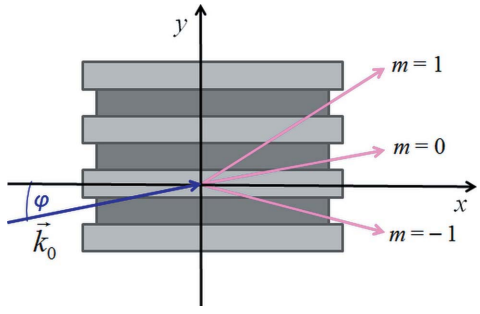

Figure 3
Projection, on the xy plane (*cf.* Fig. 1), of the incident and reflected neutron wavevectors. Owing to non-perfect alignment or beam divergence, neutrons are incident on the walls of the grating at an angle φ, and scatter in different directions depending on their diffraction order, m.

(Fig. 2). Even though neutrons are incident almost parallel to the lines of the grating (designated as the x axis in Fig. 1), our neutron beam has a finite divergence so we need to account for incident neutrons that make a nonzero angle φ with the x axis in the xy plane (Fig. 3). However, both θ and φ are a fraction of a degree in our experiments, which validates the approximations in equation (3). Note that the orientation of the coordinate axes does *not* depend on the direction of the incident beam. Besides, it should be mentioned that the tight beam collimation that we use in our experiments does not contradict the fact that SERGIS measurements can be made with loose beam collimation without any loss of resolution on the y component of the wavevector transfer, as discussed before.

To solve equation (2), we divide our system based on the scattering potential distribution into three layers: air with zero potential; a modulated air–silicon layer with a periodic potential in the region of the grating features; and a bulk silicon substrate with a constant scattering potential, such that

$$\text{air}: \quad 0 < z; \qquad \rho(\mathbf{r}) = 0, \tag{4a}$$

$$\text{mod}: \quad -t < z < 0; \quad \rho(\mathbf{r}) = \rho_{\text{mod}}(y) = \rho_{\text{mod}}(y + d), \tag{4b}$$

$$\text{sub}: \quad z < -t; \quad \rho(\mathbf{r}) = \rho_{\text{silicon}}. \tag{4c}$$

Since the Hamiltonian of equation (2) is separable, the eigenstates of equation (2) can be expressed as a product of three eigenstates for the one-dimensional motion in x, y or z. In air and the substrate, the full eigenstates are simply three-dimensional plane waves, which we shall refer to as beams. In the modulated layer, the variation of the potential along the y axis implies that the eigenstates for the y motion are one-dimensional Bloch waves, which may be written as

$$\chi_n(y) = \exp(ik_{0y}y) \sum_m b_{n,m} \exp(imgy) \tag{5}$$

where $g = 2\pi/d$ is the smallest reciprocal-lattice vector of the grating profile and $b_{n,m}$ are Bloch wave coefficients to be determined later. The associated eigenvalues, $E_{n,y}$, satisfy the one-dimensional Schrödinger equation

$$\left[-\frac{\mathrm{d}^2}{\mathrm{d}y^2} + 4\pi\rho_{\text{mod}}(y)\right]\chi_n(y) = \frac{2M}{\hbar^2}E_{n,y}\chi_n(y). \tag{6}$$

To calculate $E_{n,y}$ and $b_{n,m}$ it is convenient to expand the scattering length density in terms of its Fourier components such that

$$\rho_{\text{mod}}(y) = \sum_l \rho_l^{\text{mod}} \exp(ilgy). \tag{7}$$

For the rectangular grating profile that we consider here, the scattering length density in the modulated layer depends only on y such that

$$\frac{\rho_{\text{mod}}(y)}{\rho_{\text{silicon}}} = \begin{cases} 1, & |y| < fd/2, \\ 0, & fd/2 < |y| < d/2, \end{cases} \tag{8}$$

where f is the filling factor and $\rho_{\text{silicon}} = 2.06 \times 10^{-4}$ nm^{-2}. Thus

$$\rho_l^{\text{mod}} = \frac{1}{d}\int_{-d/2}^{d/2} \mathrm{d}y \exp(-ilgy)\rho_{\text{mod}}(y) = \frac{\rho_{\text{silicon}}}{l\pi}\sin(fl\pi) \tag{9}$$

with $\rho_0^{\text{mod}} = f\rho_{\text{silicon}}$. In the case of a grating with a rectangular profile, which we consider here, the filling factor is independent of z. Our experiments were performed on a grating with $f = 1/2$, which makes all the even Fourier coefficients, other than ρ_0^{mod}, vanish, but the theory applies equally well to other filling factors. For grating profiles with tilted or curved walls such as triangular or sinusoidal profiles, the system has to be divided into thin slices within which the approximation of vertical wall boundaries is valid. The scattering length density has the same periodicity within all slices but the filling factor changes from one slice to the next, yielding different Fourier coefficients, ρ_l^{mod}, in each slice.

With the above definitions, substituting the wavefunction, $\chi_n(y)$, and the Fourier expanded scattering length density in equation (6) leads to the secular equations

$$\left[\left(k_{0y} + mg\right)^2 + 4\pi\rho_0^{\text{mod}} - \frac{2M}{\hbar^2}E_{n,y}\right]b_{n,m} + 4\pi\sum_{p\neq m}\rho_{m-p}^{\text{mod}}b_{n,m} = 0. \tag{10}$$

The index m varies between $-m_0$ and m_0, where m_0 is an integer that defines the level at which the calculation is truncated. There will be $(2m_0 + 1)$ different eigensolutions and hence $(2m_0 + 1)$ different values of n, the index which labels both eigenvalues and eigenstates.

Based on the above discussion we can now build the total neutron wavefunction for our scattering problem. Since the grating is translationally invariant in the **x** direction, scattering from the grating will not change the x component of the neutron wavevector and we can limit our calculations to the yz plane. The y periodicity of the potential in the modulated layer determines the possible y components of the wavevectors both in air and in the substrate. Specifically, this periodicity implies that the y component of the wavevector transfer is quantized, *i.e.* is an integer multiple of g. In air, we will have an incident beam and a collection of reflected beams, while in the substrate only transmitted beams are possible, assuming that the substrate is infinitely thick so there are no reflected beams within it. In the modulated layer, we must allow for neutron beams moving in both $\pm\hat{\mathbf{z}}$ directions. With these constraints, the neutron wavefunctions in the different layers of the grating are expressed as

$$\psi_{\text{air}} = \exp(-ik_{0z}z)\exp(ik_{0y}y) + \sum_m R_{0,m}\exp(ip_{0,m}z)\exp(imgy) \times \exp(ik_{0y}y), \tag{11a}$$

$$\psi_{\text{mod}} = \sum_{n,m}\{R_{1,n}\exp[ip_{1,n}(z + t)] + T_{1,n}\exp(-ip_{1,n}z)\}b_{n,m} \times \exp(imgy)\exp(ik_{0y}y), \tag{11b}$$

$$\psi_{\text{sub}} = \sum_m T_{2,m}\exp[-ip_{2,m}(z + t)]\exp(imgy)\exp(ik_{0y}y). \tag{11c}$$

The coefficients R and T in equations (11a), (11b) and (11c) are the reflection and transmission amplitudes that describe beams propagating (or decaying) along $\pm\hat{\mathbf{z}}$, respectively. We represent the z component of the neutron wavevector by $p_{0,m}$ in air, $p_{1,n}$ in the modulated layer and $p_{2,m}$ in the substrate. The conservation of energy condition specifies the p parameters to be

$$p_{0,m} = [k_{0y}^2 + k_{0z}^2 - (k_{0y} + mg)^2]^{1/2}, \tag{12a}$$

$$p_{1,n} = \left(k_{0y}^2 + k_{0z}^2 - \frac{2M}{\hbar^2}E_{n,y}\right)^{1/2}, \tag{12b}$$

$$p_{2,m} = [k_{0y}^2 + k_{0z}^2 - (k_{0y} + mg)^2 - 4\pi\rho_{\rm silicon}]^{1/2}. \tag{12c}$$

We choose the p parameters to be either positive real or positive imaginary when their squares are either positive or negative, respectively. In writing the expressions of the neutron wavefunctions in equations (11a), (11b) and (11c), we have inserted a (+) or (−) depending on the direction of z motion that we wish to describe. With these choices we avoid the unphysical situation of waves growing exponentially as they move away from the grating in air and in the substrate. The exponentials in z in equations (11a), (11b) and (11c) have magnitudes less than unity for any value of z within the corresponding region. In equation (11b), it is very important to distinguish between n which stands for the band index (*i.e.* labels a particular eigensolution) and m, the plane wave index. The term 'band index' is used because each z component, $p_{1,n}$, of the neutron wavevector corresponds to an independent eigenstate, χ_n, of the Schrödinger equation (6) (Ashcroft & Mermin, 1976). Since each Bloch wave in the modulated layer is a sum of plane waves [*i.e.* a sum of terms in $\exp(imgy)$], we restrict the sums over beams in air and the substrate to include the same plane waves.

To obtain a complete expression of the neutron wavefunction we have to find the amplitudes R and T in each of the layers. These are calculated by applying the condition of continuity of the wavefunction and its z derivative at the air/modulated-layer interface ($z = 0$) and at the modulated-layer/substrate interface ($z = -t$). These requirements yield four sets of equations:

$$1 + \sum_m R_{0,m}\exp(imgy) = \sum_{n,m}[R_{1,n}\exp(ip_{1,n}t) + T_{1,n}] \times b_{n,m}\exp(imgy), \tag{13a}$$

$$-k_{0z} + \sum_m p_{0,m}R_{0,m}\exp(imgy) = \sum_{n,m} p_{1,n}[R_{1,n}\exp(ip_{1,n}t) - T_{1,n}] \times b_{n,m}\exp(imgy), \tag{13b}$$

$$\sum_{n,m}[R_{1,n} + T_{1,n}\exp(ip_{1,n}t)]b_{n,m}\exp(imgy) = \sum_m T_{2,m}\exp(imgy), \tag{13c}$$

$$\sum_{n,m} p_{1,n}[R_{1,n} - T_{1,n}\exp(ip_{1,n}t)]b_{n,m}\exp(imgy) = -\sum_m p_{2,m}T_{2,m}\exp(imgy). \tag{13d}$$

Equations (13a), (13b), (13c) and (13d) have to be solved so that the total y dependence summed over all of the bands is the same on both sides of a given equation. Under this condition, the R and T parameters are the solutions of the following equations:

$$\delta_{0,m} + R_{0,m} = \sum_n [R_{1,n}\exp(ip_{1,n}t) + T_{1,n}]b_{n,m}, \tag{14a}$$

$$-k_{0z}\delta_{0,m} + p_{0,m}R_{0,m} = \sum_n p_{1,n}[R_{1,n}\exp(ip_{1,n}t) - T_{1,n}]b_{n,m}, \tag{14b}$$

$$\sum_n [R_{1,n} + T_{1,n}\exp(ip_{1,n}t)]b_{n,m} = T_{2,m}, \tag{14c}$$

$$\sum_n p_{1,n}[R_{1,n} - T_{1,n}\exp(ip_{1,n}t)]b_{n,m} = -p_{2,m}T_{2,m}. \tag{14d}$$

It should be noted that the exponential term, $\exp(ip_{1,n}t)$, that appears in equations (14a), (14b), (14c) and (14d) always has, by our sign choices, a magnitude less than unity, which helps avoid numerical instabilities. For an approximation in which $|m| < m_0$, which we refer to as a $(2m_0 + 1)$ beam approximation, there are a total of $4(2m_0 + 1)$ equations for the $(2m_0 + 1)$ values for each of the four reflection and transmission amplitudes. Our aim is to calculate the reflection and transmission coefficients for each 'allowed' beam. Beams are disallowed if their associated $p_{0,m}$ or $p_{2,m}$ are imaginary. Although we keep all $(2m_0 + 1)$ beams in the boundary condition calculation, only those with real wavevector z components, propagating away from the grating, contribute to the reflectivities and transmissivities defined, respectively, by (Pendry, 1974)

$$\Re_m = \frac{p_{0,m}}{k_{0z}}\left|R_{0,m}\right|^2, \tag{15a}$$

$$\Im_m = \frac{p_{2,m}}{k_{0z}}\left|T_{2,m}\right|^2. \tag{15b}$$

They obey the conservation of flux condition (Schaich, 1978)

$$1 = \tilde{\sum_m}\,\Re_m + \tilde{\sum_m}\,\Im_m, \tag{16}$$

which is an exact result for wavefunctions of the form given by equations (11a), (11b) and (11c). Here the ($\sim$) sign on the sum is a reminder to include only 'allowed' beams. Equation (16) allows us to interpret $\Re_m$ and $\Im_m$ as probabilities describing the emerging diffracted and transmitted beams, respectively.

In Fig. 4, we plot in an extended zone scheme the band structure associated with the y motion of the neutron within the grating. To simplify the presentation we use dimensionless quantities: the wavevector k_{0y} scaled by $g/2 = \pi/d$ and the energy $E_{n,y}$ of equation (6) scaled by the energy, $(\hbar^2/2M)(g/2)^2$, of a free neutron with wavevector $g/2$. Band gaps appear at integer multiples of $2k_{0y}/g$ and they get smaller

as k_{0y} increases. To even produce these gaps for large k_{0y} we need to increase m_0 sufficiently to include the plane waves with wavevectors $k_{0y} - m_0 g \simeq -k_{0y}$ in equation (11*b*). The splitting of the near degeneracy of any two such states, with comparable magnitudes of the wavevectors, is responsible for the appearance of the gaps. The scaled value of the potential of bulk silicon is

$$v_{\rm silicon} = \frac{2\pi\hbar^2\rho_{\rm silicon}/M}{\hbar^2(g/2)^2/2M} = 4\rho_{\rm silicon}d^2/\pi \cong 5.14. \qquad (17)$$

Using equation (9), one expects in the simplest perturbation theory (Ashcroft & Mermin, 1976) a gap at the first zone boundary of $v_1 = 2v_{\rm silicon}/\pi = 3.27$, while the exact numerical calculation using the theory we have outlined yields a scaled energy of 3.06 for the first gap.

Since the lowest band in Fig. 4 is so flat, a tight-binding model (Ashcroft & Mermin, 1976) might be a relevant approximation. Indeed, if we look for bound states of a neutron in an isolated groove in silicon of width fd = 70 nm and depth t = 65 nm, we find one (even parity) bound state and its scaled energy is 1.57, which is within the energies of the lowest band in Fig. 4. Thus, at small values of k_{0y} (*i.e.* small values of φ), the neutron wavefunction, in the modulated region, should be a coherent sum of bound-state eigenfunctions. We show in Fig. 5 that the neutron wavefunction at φ = 0° has peaks within the grooves of the grating. In Fig. 6, a comparison of the density profiles of the neutron wavefunction across the grooves, calculated by the dynamical theory and by the tight-binding model, indicates that the latter gives a reasonable picture of the neutron behavior in the grooves. It should be mentioned that the single-bound-state picture will only be relevant if the separation between the grooves is wide enough to prevent significant tunneling between neighboring grooves. Of course, the full dynamical theory can account for such effects. It is also worth noting that the squared wavefunction is amplified, within the grooves, by more than an order of magnitude with respect to the incident beam (plane wave with unit modulus), for the parameters used in Fig. 6, and even larger increases may be possible for different configurations. The fact that the wavefunction peaks in the grating channels indicates that the channels can act as waveguides for neutrons, an effect similar to the guiding of neutrons through thin layers that has been observed in the past (Feng *et al.*, 1994).

To understand the scattering process it is instructive to study the behavior of the reflectivities as a function of the tilt

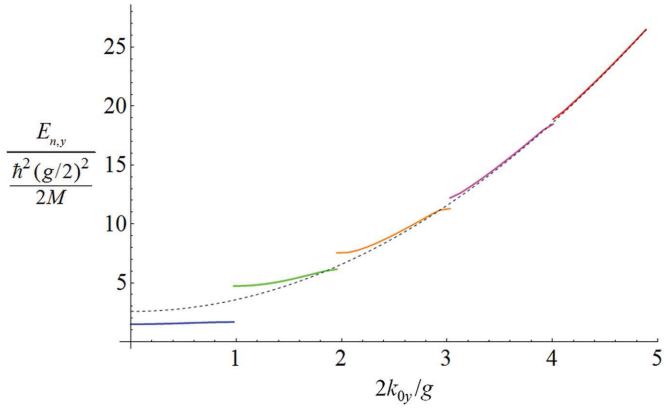

Figure 4
Extended zone scheme representation of the band structure of neutrons (with λ = 0.5 nm and θ = 0.2°) scattered by a grating (with d = 140 nm, f = 0.5 and t = 65 nm) (solid lines). There are band gaps at zone boundaries at integer multiples of $2k_{0y}/g$. The band gap is large at the first zone boundary and gets smaller as k_{0y} increases. The dashed line represents the scaled kinetic energy, $E_{\rm av}$, of a neutron moving in a homogeneous medium with an average scattering length density $\rho_{\rm silicon}/2$. At large k_{0y}, the Bloch energy is well approximated by $E_{\rm av}$.

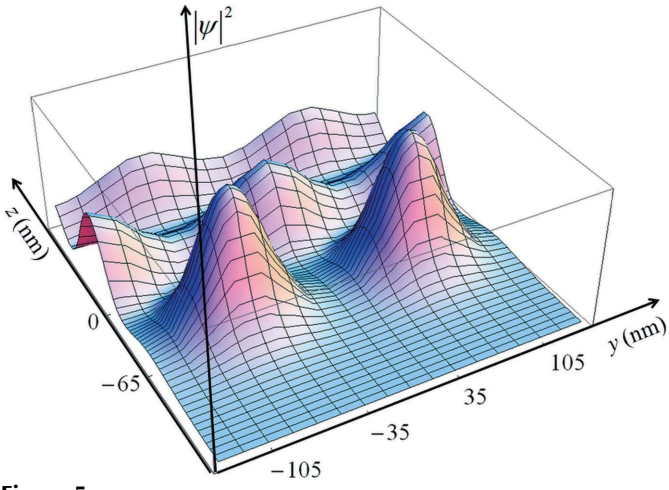

Figure 5
Plot of the modulus squared of the neutron wavefunction (with λ = 0.5 nm) in the different layers of the grating at a grazing angle θ = 0.2° in the case of perfect alignment of the grating with the neutron beam, *i.e.* φ = 0°. The wavefunction peaks in the grooves of the grating located in the regions $-105 < y < -35$ and $35 < y < 105$ in the modulated layer which lies between z = 0 nm and z = −65 nm. This behavior of the wavefunction indicates the possibility of guiding neutrons along the grooves.

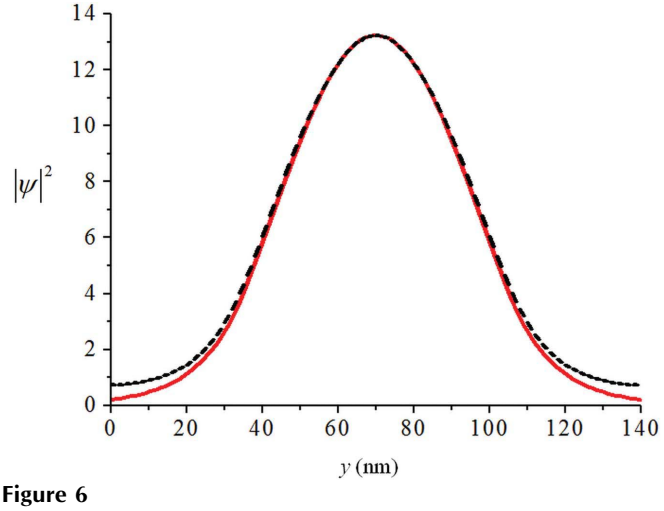

Figure 6
Plot of the modulus squared of the neutron wavefunction at z = −45 nm (for λ = 0.5 nm and θ = 0.2°) as calculated by the dynamical theory (dashed line) for φ = 0°, and by the tight-binding approximation (solid line) across an isolated groove in the grating located in the region $35 < y < 105$. The dynamical theory result is normalized to unit modulus of the incident beam while the bound-state wavefunction is scaled to match the maximum density of the dynamical theory wavefunction.

angle φ, or the wavevector k_{0y} related by equation (3). In Fig. 7, we plot the allowed reflectivities $\Re_m$.

An Ewald construction provides a pictorial representation of the energy and momentum constraints on the scattering process. For elastic scattering, the wavevectors of the incident and the reflected waves, all of the same magnitude because of energy conservation, are drawn as radii of the Ewald circle. Owing to momentum conservation, scattering is allowed only if the tip of the scattered wavevector lies on one of the Bragg rods, which are the vertical dashed lines in Fig. 8. These Bragg rods are equally spaced by g and indexed by m with the tip of the incident wavevector touching the $m = 0$ rod. The sign of the z component of the scattered wavevectors must be opposite to that of the incident wavevector. The number of Bragg rods that intersect the energy-conserving circle determines the number of allowed beams. In a typical case of a neutron of wavelength 0.5 nm, incident on the grating at a grazing angle $\theta = 0.2^\circ$ and in perfect alignment with the grooves, *i.e.* $\varphi = 0^\circ$ or $k_{0y} = 0$, the radius of the Ewald circle is $k_{0z} < g$ for our 140 nm-period grating so only specular reflection is allowed (Fig. 8*a*). As k_{0y} increases, the Ewald circle increases in radius and intersects more Bragg rods, allowing further beams with $m < 0$ to 'turn on' while keeping beams with $m > 0$ forbidden (Fig. 8*b*). For our experiments, only a few Bragg rods contribute to the scattering process. If we increase θ or decrease λ so that $k_{0z} > g$, beams of both signs of m can be allowed, starting from $k_{0y} = 0$ as shown in Fig. 8(*c*). This case was used as a basis for Figs. 2 and 3.

The threshold at which a particular beam, of index $m < 0$, first becomes allowed in Fig. 7 corresponds to the value of k_{0y} at which the Ewald circle is tangent to the mth Bragg rod. For negative values of m, this condition is satisfied when

$$\left|k_{0y} - |m|g\right| = (k_{0y}^2 + k_{0z}^2)^{1/2}, \tag{18}$$

implying a threshold value

$$2k_y^{\rm th}/g = |m| - \frac{(k_{0z}d/2\pi)^2}{|m|}. \tag{19}$$

For $\lambda = 0.5$ nm and $\theta = 0.2^\circ$, $k_{0z}d/2\pi = 1.956$ which indicates that the beams of orders $m = -1, -2, -3, \ldots$ turn on at $2k_{0y}/g \simeq 0.04, 1.52, 2.68, \ldots$, respectively, exactly equal to the 'turn on' thresholds in Fig. 7. Note that when one beam turns on, the reflectivities of already allowed beams exhibit a downward irregularity, a behavior analogous to the optical phenomenon of a Rayleigh–Wood anomaly (Hessel & Oliner, 1965). There are additional irregularities in Fig. 7 that are due to trans-

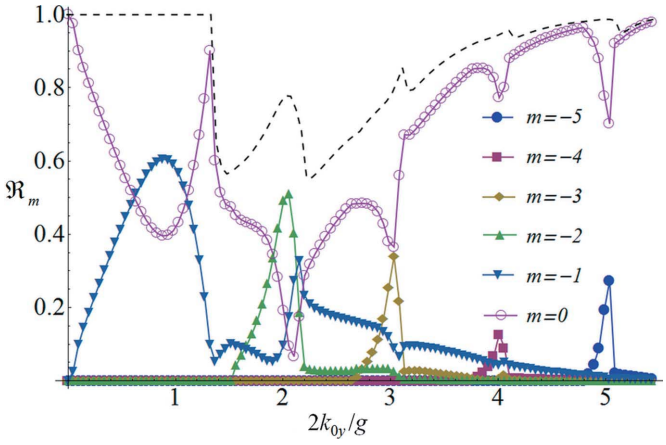

Figure 7
Plot of the reflectivities, $\Re_m$, of the different allowed beams (for $\lambda = 0.5$ nm and $\theta = 0.2^\circ$), in an 11-beam approximation. Beams of different orders 'turn on' at particular values of the incident wavevector k_{0y}. Specular reflection is dominant at very small as well as large values of k_{0y}. The dashed line is a sum of all the allowed reflectivities and is unity for values of $2k_{0y}/g$ less than 1.33, at which the first allowed transmitted beam turns on.

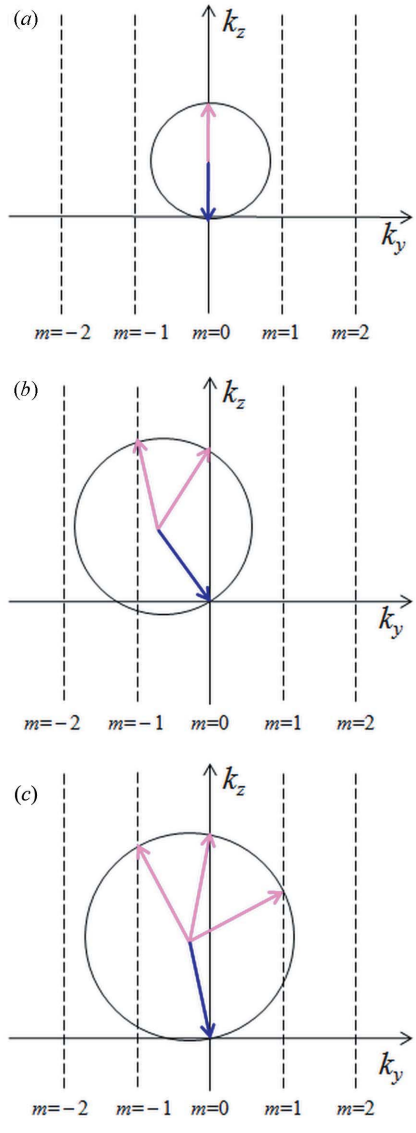

Figure 8
Ewald construction in the case (*a*) $k_{0z} < g$ and $k_{0y} = 0$ showing that only specular reflection is allowed; (*b*) $k_{0z} < g$ and $k_{0y} > 0$ where only negative m values are allowed as Bragg rods with $m > 0$ cannot be reached; (*c*) $k_{0z} > g$ and $k_{0y} > 0$ where beams of positive as well as negative values of m are allowed. Dark and light arrows (blue and pink in the electronic version of the journal) correspond to the incident and scattered wavevectors, respectively, just as in Figs. 2 and 3.

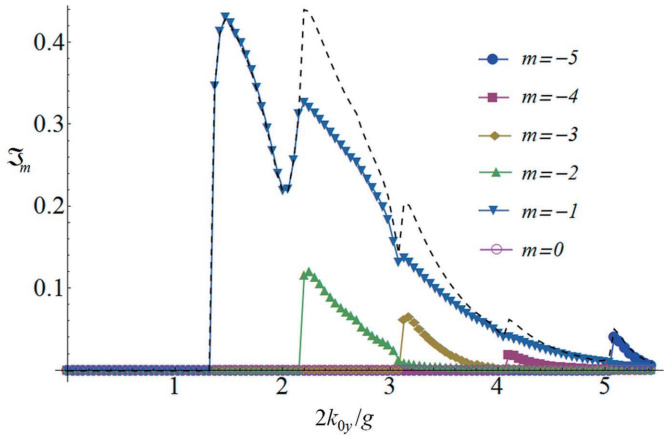

Figure 9
Plot of the transmissivity of beams of different diffraction orders in an 11-beam approximation calculated for a neutron of wavelength $\lambda = 0.5$ nm in the case of a grazing angle $\theta = 0.2°$. The sum of the transmissivities (dashed line) indicates that transmission is not allowed below a threshold value of 1.33, consistent with Fig. 7.

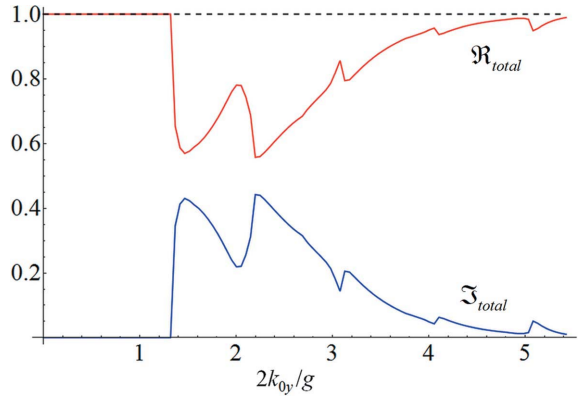

Figure 10
The total reflectivity (upper line) and the total transmissivity (lower line) (calculated for $\lambda = 0.5$ nm and $\theta = 0.2°$) sum up to unity (dashed line) for all values of $2k_{0y}/g$, confirming that neutron flux is conserved in the dynamical theory.

mitted beams being allowed, for which the energy conservation constraint is given by equation (12*c*) instead of (12*a*). Although Ewald pictures are generally no longer possible in these cases, the algebra of equations (18) and (19) still works if we simply replace $k_{0z}^2 \rightarrow k_{0z}^2 - 4\pi\rho_{\rm silicon}$. Then the threshold for a transmitted ($m < 0$) beam to turn on is

$$2k_y^{\rm th}/g = |m| - \frac{(k_{0z}d/\pi)^2 - v_{\rm silicon}}{4|m|}. \qquad (20)$$

This equation explains the origin of the remaining irregularities in the $\Re_m$ plots of Fig. 7 and reproduces the threshold values in the $\Im_m$ plots of Fig. 9. For $\lambda = 0.5$ nm and $\theta = 0.2°$, equation (20) indicates that the transmitted beams of orders $m = -1, -2, -3, \ldots$ turn on at $2k_{0y}/g \simeq 1.33, 2.16, 3.11, \ldots$, respectively. The fact that no transmitted beams are allowed below $2k_{0y}/g = 1.33$ leads to the unit total reflectivity below this threshold in Fig. 7. For larger k_{0y}, Bragg scattering in the y direction and the coupling between y and z momenta implied by the energy conservation condition [equation (12*c*)] can produce a real value of the z component of the momentum in the substrate although θ is below the critical angle for silicon, as it is for Figs. 7 and 9. It is worth remarking that no irregularities appear in the $\Re_m$ or the $\Im_m$ plots at integer values of $2k_{0y}/g$, *i.e.* at the band gaps of Fig. 4. The plots of the total reflectivity and total transmissivity in Fig. 10 confirm the conservation of flux given by equation (16).

3. SERGIS

When the SERGIS method is used to study grating reflection, one needs the relative probabilities, $\tilde{p}_m$, of the different reflected beams in order to calculate the normalized spin-echo polarization, P/P_0. These probabilities are readily determined from the allowed reflection coefficients, given by equation (15*a*), to be

$$\tilde{p}_m = \Re_m \Big/ \sum_m^{\sim} \Re_m. \qquad (21)$$

By definition, $\sum_m \tilde{p}_m = 1$. Since the normalized spin-echo polarization for a neutron scattered with wavevector transfer $q_y = mg$ is equal to $\cos(mgy_{\rm se})$, the total normalized echo polarization is given by

$$\frac{P(y_{\rm se})}{P_0} = \sum_m \tilde{p}_m \cos(mgy_{\rm se}), \qquad (22)$$

where $y_{\rm se}$ is the spin-echo length derived by Gähler *et al.* (1996) and Bouwman *et al.* (2002):

$$y_{\rm se} = 2\frac{\mu B}{E_0} L \cot\alpha = (1.476 \times 10^{14}\,{\rm T^{-1}m^{-2}}) LB\lambda^2 \cot\alpha. \qquad (23)$$

Here L is the separation between the centers of the magnetic field regions used in the SERGIS experiments, B is the magnitude of the magnetic field at the interface between these field regions (Pynn *et al.*, 2009) and α is the orientation of the boundary of the magnetic regions with respect to the neutron beam direction (Fig. 11). The ratio in equation (23) involves

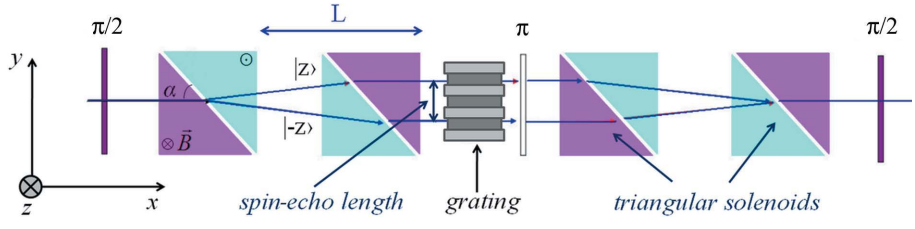

Figure 11
Diagram of the SERGIS setup. The different shades of the triangles in each triangle-pair represent oppositely directed magnetic fields along the z direction. As the neutron beam enters the first $\pi/2$ flipper from the left it is split into two coherent sub-beams of opposite spin states that follow different trajectories, as indicated in the figure. The two sub-beams serve as probes that scan the surface structure of the sample along the desired (y) direction.

E_0, the neutron's kinetic energy in vacuum, and μB, the magnitude of the Zeeman energy of a polarized neutron in a magnetic field (μ is the neutron magnetic moment). It should be noted that equation (22) is equivalent, in reflection mode, to the conventional expression of the normalized spin-echo polarization (Rekveldt *et al.*, 2005):

$$\frac{P(y_{se})}{P_0} = \frac{\int \frac{d\sigma}{d\Omega}(q_y)\cos(q_y y_{se})d\Omega}{\int \frac{d\sigma}{d\Omega}(q_y)d\Omega}, \qquad (24)$$

where q_y is the y component of the wavevector transfer. Equations (22) and (24) hold for a single ray within the incident beam, *i.e.* for a definite value of φ, so to compare with the experimental results we need to average over φ. In our experiments, the detector captures reflected neutrons with all values of k_y generated by the grating so there is no further limitation on the sum over m in equation (22).

The SERGIS apparatus we use, which is an implementation of spin-echo scattering angle measurement to GISANS, has been described a number of times before (Pynn *et al.*, 2005, 2009) and is shown schematically in Fig. 11. The apparatus serves to split a neutron wavefunction into two spin states, denoted $|z>$ and $|-z>$ in Fig. 11, that propagate with strong mutual coherence. If the sample reflects only specularly, the symmetry of the assembly of the magnetic triangles shown in Fig. 11 causes the two neutron spin states to exit the secondary flight path (at the right of Fig. 11) with the same acquired phase, having undergone identical trajectories. More precisely the relative phase between the two states acquired in the first half of the setup, before the sample, is counterbalanced in the second half so that the two states emerge without any Larmor phase difference. Consequently, the incident beam polarization is retrieved as spin echo. If the sample scatters in the **y** direction, neutrons move along different trajectories in the second half of the apparatus and symmetry is lost. The polarization of the emerging beam is then related to the Larmor phase difference through equation (22). Explicitly, the normalized echo polarization, P/P_0, is the sum over all possible wavevector transfers of a weighted average of the cosine of the net Larmor phase difference between the neutron spin states.

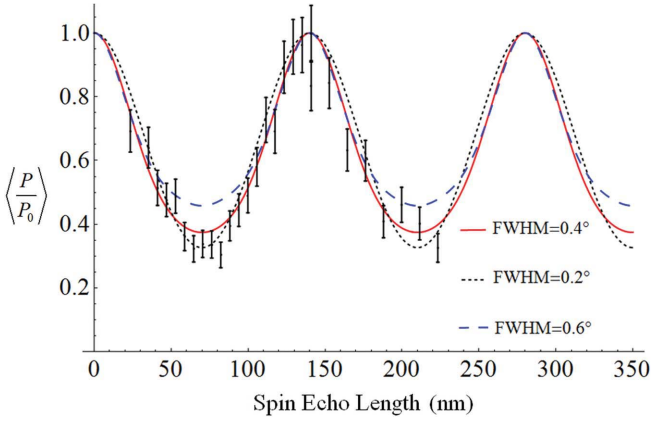

Figure 12
Plots of the SERGIS polarization, calculated for different incident beam divergences, at the fixed-wavelength beamline AND/R at NCNR. The smooth curves are based on an 11-beam approximation ($m_0 = 5$) and show a periodic behavior of the echo polarization as a function of the spin-echo length, peaking to unity at integer multiples of d. The depth of the dips changes with the beam divergence. The experimental value of the beam divergence (0.4° FWHM) gives a reasonable fit (solid line) to the data points within the measured error bars. The sensitivity of the result to beam divergence is illustrated by the calculated curves for divergences of 0.2 and 0.6°.

4. Data analysis

The same SERGIS hardware was used to study the same diffraction grating on two different neutron beamlines: the AND/R fixed-wavelength beamline at the continuous wave (CW) neutron source at NCNR, and the ASTERIX variable-wavelength beamline at the pulsed neutron source at LANSCE. The spin-echo polarization was measured as a function of the spin-echo length in both cases. Both sets of data showed a similar behavior of the spin-echo polarization which peaked at integer multiples of the grating period, but some differences were observed when the results were examined in detail.

4.1. SERGIS at a CW source

At AND/R with a neutron beam of fixed wavelength (λ = 0.5 nm), the spin-echo length could be varied either by varying the separation distance between the triangular electromagnets or by varying the magnetic field strength at their interfaces. In our experiment, we scanned the spin-echo length by varying the electric current, I, in the triangular solenoids, providing a variable magnetic field in the triangular coils. For current values between 1 and 10 A the spin-echo length ranges from ~23 to ~230 nm. The spin-echo polarization measured with our grating (Fig. 12) shows a periodic behavior as a function of the spin-echo length, peaking to unity at integer multiples of the grating period d. The dynamical theory predicts that the echo polarization is a periodic function of the spin-echo length because it yields a result that is the weighted sum of cosine functions with a common period, d, in y_{se}. The arguments of the cosine functions in equation (22) do not depend on φ, while the weighting functions are set by the reflectivities, $\Re_m$, which do depend on φ but not on y_{se} (for a fixed value of λ). Hence an average over φ does not change the periodicity of the spin-echo polarization. From the discussion of the reflectivities presented in §2, we can determine what range of reflected beams contributes for a given incident beam divergence. The plot in Fig. 13 of $\tilde{p}_m$ along with the distribution of possible φ values shows that the beams of orders down to $|m|$ = 3 should be included. Nevertheless, since the lower-order beams (m = 0, ±1) make the dominant contribution in the scattering process, we find P/P_0 to be close to a simple cosine-like function just as our data indicate. Not surprisingly, given the strong dependence of the reflectivities on φ depicted in Fig. 7, the amplitude of the periodic SERGIS polarization is dependent on the width in φ of the incident beam. With the slit geometry that we had for the AND/R experiment, the beam

divergence in φ is 0.4° FWHM. The dynamical theory calculation, with all the parameters (incident angles, beam divergence, neutron wavelength and sample dimensions) set to their experimentally measured values, provides a good description of the measured echo polarization as shown in Fig. 12; in particular, the amplitude and shape of the polarization oscillation are correctly accounted for. The averaged form of equation (22), for a fixed value of λ, is

$$\left\langle \frac{P(y_{se})}{P_0} \right\rangle = \sum_m \langle \tilde{p}_m \rangle \cos(m g y_{se}). \qquad (25)$$

Using the experimental value of the FWHM we obtain $\langle \tilde{p}_m \rangle \simeq 0.63, 0.15, 0.03, 0.004$ for $|m| = 0, 1, 2, 3$, respectively. The dominance of the first three $\langle \tilde{p}_m \rangle$ values (corresponding to $m = 0, \pm 1$) accounts for the near cosine-like shape of the oscillation in Fig. 12.

4.2. SERGIS at a pulsed source

At ASTERIX, the current in the triangles need not be changed because the spin-echo length varies with the variable wavelength of the neutron beam ($0.4 < \lambda < 0.9$ nm), which is determined using time of flight. With the current in the triangular electromagnets fixed at 12 A, the spin-echo length ranges between ∼90 and ∼450 nm. Again, the measured spin-echo polarization, shown in Fig. 14, peaks at integer multiples of the grating period but the echo polarization is not a periodic function of the spin-echo length as in Fig. 12. The dynamical theory explains the loss of periodicity by the fact that $\tilde{p}_m$ depends on λ and hence on y_{se}, so the weight factors in equation (22) have a nonperiodic variation in y_{se}. The incident beam divergence that we use in the analytical calculations is a Gaussian distribution in φ of 0.19° FWHM (corresponding to the experimental value) and offset $\varphi_0 = 0.09°$. It should be mentioned that the alignment of the grating with the neutron beam was not determined to better than 0.1° and our choice of φ_0, within the experimental uncertainty in average alignment, provides the best fit to our data.

At small spin-echo lengths we observe a number of sharp features in the theoretical curve. The ones that first appear as y_{se} decreases are remnants (in the sense of surviving the average over φ) of the Rayleigh–Wood anomalies. In particular, the sharp peak at $y_{se} \simeq 102$ nm is due to the onset of the $m = 0$ transmission, whereas the irregularities at spin-echo lengths between 40 and 60 nm arise from the thresholds of higher-order transmitted beams. At still smaller y_{se}, the $m = 0$ transmission rises to more than 90% and all the reflection and other transmission coefficients become quite small (although the relative probabilities, $\tilde{p}_m$, are not). In this limit any kind of scattering is very weak and the reflectivities are primarily determined by the interference of waves reflected from either the top or the bottom of the modulated layer. The variation of the phase difference between these two waves is controlled in the small-wavelength limit by $2k_{0z}t$. In addition, our numerical results indicate that the interference oscillations due to the $m = 0$ or the $|m| = 1$ pair of reflected waves are out of phase with each other. Consequently, $R_{0,0}$ and $R_{0,\pm1}$ oscillate out of phase relative to each other with a period set by $2k_{0z}t$ = integer. This argument explains the series of peaks and dips occurring at spin-echo lengths smaller than 20 nm.

5. Concluding remarks

The dynamical theory calculation has proven to be successful in describing neutron reflection from a grating with periodic structure and a simple profile. It explains the differences in the SERGIS polarization we observed at two different neutron

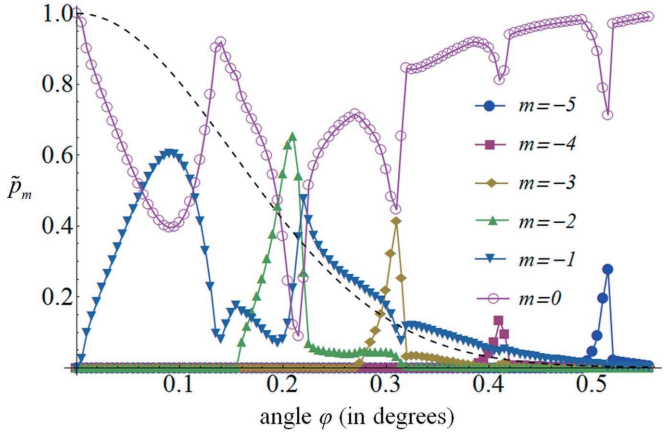

Figure 13
Plot of the relative probabilities as a function of the tilt angle φ. The angular distribution of the incident neutron beam is a Gaussian in φ with FWHM = 0.4° (dashed line) and offset $\varphi_0 = 0$. Within this incident beam divergence, reflected beams of orders $m = 0$ and $m = \pm 1$ make the dominant contribution. Note that this plot depicts the behavior of the reflectivities in terms of positive values of φ only. For negative values of φ, the plots of the reflectivities of positive orders are obtained from their negative-order counterparts by symmetry with respect to the vertical axis.

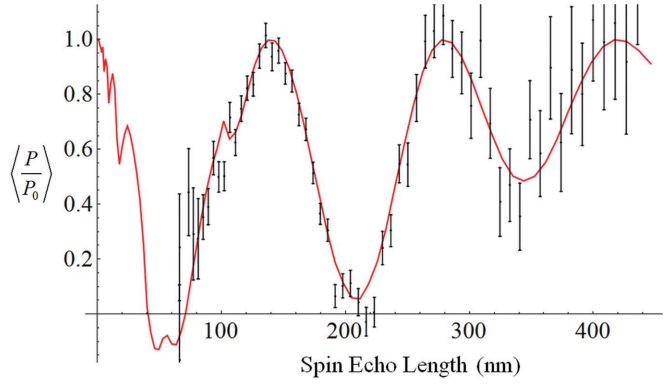

Figure 14
Plot of the SERGIS polarization measured using the ASTERIX reflectometer at the LANSCE pulsed neutron source (data points with experimental error bars) compared with the dynamical theory truncated to $m_0 = 9$ (solid line) calculated for a Gaussian distribution in φ with FWHM = 0.19° and offset $\varphi_0 = 0.09°$. The large value of m_0 is required because at small wavelengths the Ewald circle grows larger, hence more beams contribute to the scattering process. The peaks and dips in the measured polarization are the same as predicted by the dynamical theory and appear, as expected, at integer and half-integer multiples of the grating period. The nonperiodic structure of the echo polarization is due to the wavelength dependence of the reflectivities and the spin-echo length.

sources and the importance of the divergence of the incident neutron beam perpendicular to the specular reflection plane (φ) as well as the neutron wavelength and the grazing-incident angle θ in determining the precise pattern that is observed. The calculation is in very good agreement with the experimental results when all the parameters used in the theory (beam divergence, incident angle, sample features, size *etc.*) are set to their experimentally measured values. The calculation also serves as an instructive method to visualize the behavior of the neutron wavefunction in the vicinity of gratings. It illustrates the guiding of neutrons along the grooves of the grating for particular incidence conditions, as well as various resonance phenomena which, while not surprising, have not yet been observed with neutrons to our knowledge, although the guiding of neutrons has been observed in simple layered systems (Feng *et al.*, 1994). Based on this calculation, we expect to be able to calculate, using a perturbation method, the scattering from material deposited in the grooves of a grating and intend to apply the method in the future to study the directed self assembly of various macromolecules aligned in the grooves of a diffraction grating.

This work was supported by the US Department of Energy through its Office of Basic Energy Sciences, Division of Material Science and Engineering (grant No. DE-FG02-09ER46279). The NIST Center for Neutron Research, where one of the experiments described here was performed, is funded by the US Department of Commerce. The Los Alamos Neutron Science Center, where the other experiment was carried out, is operated by the US Department of Energy. The authors thank the staff of both facilities for their assistance.

References

Ashcroft, N. W. & Mermin, N. D. (1976). *Solid State Physics.* New York: Holt, Rinehart and Winston.
Berrouane, H., André, J. M., Barchewitz, R., Moreno, T., Sammar, A., Khan Malek, C., Pardo, B. & Rivoira, R. (1992). *Nucl. Instrum. Methods Phys. Res. Sect. A*, **312**, 521–530.
Bethe, H. A. (1928). *Ann. Phys. Amsterdam Neth.* **87**, 55–129.
Bouwman, W. G., Kruglov, T. V., Plomp, J. & Rekveldt, M. T. (2005). *Phys. B (Amsterdam)*, **357**, 66–72.
Bouwman, W. G., Uca, O., Grigoriev, S. V., Kraan, W. H., Plomp, J. & Rekveldt, M. T. (2002). *Appl. Phys. A Mater. Sci. Process.* **74**, s115–s117.
Cowley, J. M. & Moodie, A. F. (1957). *Acta Cryst.* **10**, 609–619.
Cowley, J. M. & Moodie, A. F. (1959). *Acta Cryst.* **12**, 360–367.
Felcher, G. P., teVelthuis, S. G. E., Major, J., Dosch, H., Anderson, C., Habicht, K. & Keller, T. (2002). *Proc. SPIE*, **4785**, 164–174.
Feng, Y. P., Majkrzak, C. F., Sinha, S. K., Wiesler, D. G. & Zhang, H. (1994). *Phys. Rev. B*, **49**, 10814–10817.
Gähler, R., Golub, R., Habicht, K., Keller, T. & Felber, J. (1996). *Phys. B Condens. Matter*, **229**, 1–17.
Haan, V.-O. de, Plomp, J., Bouwman, W. G., Trinker, M., Rekveldt, M. T., Duif, C. P., Jericha, E., Rauch, H. & van Well, A. A. (2007). *J. Appl. Cryst.* **40**, 151–157.
Hessel, A. & Oliner, A. A. (1965). *Appl. Opt.* **4**, 1275–1297.
Hu, X., Jiao, X., Narayanan, S., Jiang, Z. K., Sinha, S., Lurio, L. B. & Lal, J. (2005). *Eur. Phys. J. E Soft Matter Biol. Phys.* **17**, 353–359.
Humphreys, C. J. (1979). *Rep. Prog. Phys.* **42**, 1826–1887.
Jap, B. K. & Glaeser, R. M. (1978). *Acta Cryst.* A**34**, 94–102.
Krouglov, T., de Schepper, I. M., Bouwman, W. G. & Rekveldt, M. T. (2003). *J. Appl. Cryst.* **36**, 117–124.
Major, J., Vorobiev, A., Rühm, A., Maier, R., Major, M., Mezger, M., Nülle, M., Dosch, H., Felcher, G. P., Falus, P., Keller, T. & Pynn, R. (2009). *Rev. Sci. Instrum.* **80**, 123903.
Maystre, D. & Petit, R. (1972). *Opt. Commun.* **5**, 90–93.
Neviere, M., Vincent, P. & Petit, R. (1974). *Nouv. Rev. Opt.* **5**, 65–77.
Ott, F., Humbert, P., Fermon, C. & Menelle, A. (2001). *Phys. B (Amsterdam)*, **297**, 189–193.
Parratt, L. G. (1954). *Phys. Rev.* **95**, 359–369.
Pendry, J. B. (1974). *Low Energy Electron Diffraction: the Theory and its Application to Determination of Surface Structure.* New York: Academic Press.
Plomp, J. (2009). PhD thesis, Delft University of Technology, The Netherlands.
Plomp, J., de Haan, V. O., Dalgliesh, R. M., Langridge, S. & van Well, A. A. (2007). *Phys. B (Amsterdam)*, **397**, 76–78.
Pynn, R. (1992). *Phys. Rev. B*, **45**, 602–612.
Pynn, R., Fitzsimmons, M. R., Fritzsche, H., Gierlings, M., Major, J. & Jason, A. (2005). *Rev. Sci. Instrum.* **76**, 053902.
Pynn, R., Fitzsimmons, M. R., Lee, W. T., Stonaha, P., Shah, V. R., Washington, A. L., Kirby, B. J., Majkrzak, C. F. & Maranville, B. B. (2009). *Phys. B (Amsterdam)*, **404**, 2582–2584.
Rekveldt, M. T., Plomp, J., Bouwman, W. G., Kraan, W. H., Grigoriev, S. & Blaauw, M. (2005). *Rev. Sci. Instrum.* **76**, 033901.
Schaich, W. L. (1978). *Photoemission in Solids I*, pp. 105–134. Berlin: Springer.
Sinha, S. K., Sirota, E. B., Garoff, S. & Stanley, H. B. (1988). *Phys. Rev. B*, **38**, 2297–2311.
Vogt, B. D., Lee, H.-J., Wu, W.-l. & Liu, Y. (2005). *J. Phys. Chem. B*, **109**, 18445–18450.
Zabel, H. (1994). *Appl. Phys. A*, **58**, 159–168.